RESEARCH ARTICLE

Magnetic Resonance in Medicine

Effects of prospective motion correction on perivascular spaces at 7T MRI evaluated using motion artifact simulation

Bingbing Zhao | **Yichen Zhou** | **Xiaopeng Zong**

School of Biomedical Engineering and State Key Laboratory of Advanced Medical Materials and Devices, ShanghaiTech University, Shanghai, People's Republic of China

Correspondence
Bingbing Zhao, School of Biomedical Engineering, ShanghaiTech University, 393 Middle Huaxia Road, Shanghai, People's Republic of China.
Email: zhaobb2022@shanghaitech.edu.cn

Abstract

Purpose: The effectiveness of prospective motion correction (PMC) is often evaluated by comparing artifacts in images acquired with and without PMC (NoPMC). However, such an approach is not applicable in clinical setting due to unavailability of NoPMC images. We aim to develop a simulation approach for demonstrating the ability of fat-navigator-based PMC in improving perivascular space (PVS) visibility in T_2-weighted MRI.

Methods: MRI datasets from two earlier studies were used for motion artifact simulation and evaluating PMC, including T_2-weighted NoPMC and PMC images. To simulate motion artifacts, k-space data at motion-perturbed positions were calculated from artifact-free images using nonuniform Fourier transform and misplaced onto the Cartesian grid before inverse Fourier transform. The simulation's ability to reproduce motion-induced blurring, ringing, and ghosting artifacts was evaluated using sharpness at lateral ventricle/white matter boundary, ringing artifact magnitude in the Fourier spectrum, and background noise, respectively. PVS volume fraction in white matter was employed to reflect its visibility.

Results: In simulation, sharpness, PVS volume fraction, and background noise exhibited significant negative correlations with motion score. Significant correlations were found in sharpness, ringing artifact magnitude, and PVS volume fraction between simulated and real NoPMC images ($p \leq 0.006$). In contrast, such correlations were reduced and nonsignificant between simulated and real PMC images ($p \geq 0.48$), suggesting reduction of motion effects with PMC.

Conclusions: The proposed simulation approach is an effective tool to study the effects of motion and PMC on PVS visibility. PMC may reduce the systematic bias of PVS volume fraction caused by motion artifacts.

KEYWORDS
high-field MRI, motion artifact simulation, perivascular spaces, prospective motion correction

1 | INTRODUCTION

Perivascular spaces (PVS) are identified as an essential pathway for clearing metabolic wastes in glymphatic system,[1] the abnormality of which has been found to be associated with a variety of neurovascular and neurodegenerative diseases.[2] Recent advances in high field MRI allow for the higher spatial resolution and the detec-

tion of a higher number of PVSs in vivo. However, as resolution improves, MR scans are prolonged and become more sensitive to head movements. Motion can induce blurring and ringing artifacts and additional noises in the reconstructed image,[3,4] rendering inaccuracy and unreliability of PVS measurement and reducing its diagnostic or scientific relevance.[5]

To mitigate the motion-induced artifacts, two widely used schemes including retrospective motion correction[5–9] and prospective motion correction (PMC) have been reported.[10–18] An earlier study[5] using fat navigators (FatNav) to estimate motion profile has found the beneficial effects of retrospective motion correction on measuring PVS visibility and physiological changes. However, the effectiveness of FatNav-based PMC on improving PVS visibility remains unclear.

To evaluate the performance of PMC, uncorrected reference images are required to quantify image quality improvements. Several methods have been proposed to obtain the uncorrected images,[10–18] which often require additional or prolonged scans. Motion artifact simulation can avoid additional data acquisition and is therefore a more feasible approach for evaluating PMC in clinical setting.[18]

In this work, we propose a motion artifact simulation approach that takes into account k-space acquisition process and uses artifact free multi-channel combined magnitude images and measured motion profiles. With the aid of simulated images, we studied the effects of motion and FatNav-based PMC on PVS visibility. First, we validated the veracity of motion artifact simulation by comparing four metrics that quantified the artifact level and PVS visibility between simulated images and real images without PMC. Then, we investigated the effects of PMC on image artifact level and PVS visibility by comparing real images with PMC and simulated images without PMC.

2 | METHODS

2.1 | Data acquisition and processing

2.1.1 | Participants

This study included two datasets from two earlier studies.[5,19] The first dataset included 33 healthy volunteers (aged 21–55 years, 23 females). All subjects underwent a scan during air breathing and another scan during carbogen breathing, resulting in 66 images in total.[5] No motion correction was performed; however, navigators were acquired and will be named the without PMC dataset (*NoPMC dataset*) in this study. The second dataset with the PMC-enabled, named *PMC dataset* in this study,

included 19 patients with diabetes mellitus and 19 age- and sex-matched healthy controls (aged 34–70 years, 21 females).[19]

2.1.2 | MRI protocol

All images were acquired on a 7 T MRI scanner (Siemens Healthineer, Erlangen, Germany) equipped with an eight-channel (NoPMC dataset) or a single-channel (PMC dataset) transmitter and a 32-channel receiver head coil (Nova Medical, Wilmington, MA). No B_1 shimming for reducing radiofrequency field inhomogeneity was performed when using the eight-channel transmitter.

For both datasets, a 3D variable flip angle turbo spin echo (TSE) sequence was used to acquire T_2-weighted images for imaging PVSs using the following parameters: TR/TE = 3000 (NoPMC) or 3,300 (PMC)/326 ms, field of view (FOV) = 210 × 210 × 99.2 mm³, matrix size = 512 × 512 × 248, voxel size = 0.41 × 0.4 × 0.4 mm³, axial slices, scan time = 8:03 (NoPMC) or 8:48 (PMC) min, and all k-space data at a single partition encoding (PAR) step was acquired during each TR. Partial Fourier sampling was performed with a factor of 0.79 and 0.625 along the phase encoding (PE) and PAR directions, respectively. Undersampling factor was 3 with 24 auto-calibration lines along PE direction. Oversampling factor was 0.0323 along the PAR direction.

A 3D FatNav[20] was embedded within each TR to monitor motion. With a binomial excitation pulse to selectively excite fat signal centered at 3.4 ppm upfield from water, the sequence parameters were set as follows: TR/TE = 3/1.31 ms, flip angle = 7°, undersampling factors = 4, partial Fourier factor = 0.75 along both PE and PAR directions, FOV = 220 × 220 × 180 mm³ (NoPMC) or 222 × 198 × 210 mm³ (PMC), matrix size = 100 × 100 × 82 (NoPMC) or 74 × 66 × 70 (PMC), voxel size = 2.2 × 2.2 × 2.2 mm³ (NoPMC) or 3 × 3 × 3 mm³ (PMC), axial slices and duration = 0.89 s (NoPMC) or 0.47 s (PMC). A FatNav image with fully sampled rectangular region around k-space center was acquired before the first TR for obtaining calibration data for GRAPPA reconstruction.[21]

2.1.3 | Prospective motion correction

Prospective motion correction works by dynamically modifying scanner parameters in real time according to motion data. During the scans, the FatNav images were reconstructed and then registered to the first reference image using the vendor software installed on the scanner (MOCO functor) in order to yield relative motion parameters. These parameters were transmitted to the sequence

to adjust the imaging FOV position and orientation for the next TR such that the relative position between the imaged object and the FOV remained the same throughout the scan.

2.1.4 | Image reconstruction

The TSE images were reconstructed using vendor-provided software on the scanner, and the Fat-Nav images were reconstructed using the GRAPPA algorithm.[21]

2.2 | **Motion artifact simulation**

Motion reduces image quality by introducing inconsistencies into k-space data. Due to motion, the MR signals corresponding to k-space data are placed into wrong positions in the k-space before inverse Fourier transform into the image space. Therefore, the key of motion artifact simulation is to generate the k-space data at the real positions of readout lines in non-Cartesian grid, and then rearrange them into the intended Cartesian k-space coordinates.

The simulation included the following steps: (1) Due to oversampling along the PAR direction, we expanded the initial magnitude image by zero filling four voxels on each edge such that its Fourier transform matched the sampled k-space positions. (2) The three rotational motion parameters in each TR were converted into a 3×3 matrix A for transforming the intended Cartesian k-space coordinates k to the real measured non-Cartesian coordinates k' by $k' = Ak$. (3) The magnitude images expanded by (1) were then Fourier transformed into the k-space at the real k-space coordinates k' through 3D nonuniform fast Fourier transform.[22] (4) The k-space data were "incorrectly" placed onto the predefined Cartesian coordinates k. The phase at each k-space position was adjusted according to $S'(k) = S(k') \times e^{ik \times \Delta r}$ to account for the linear phase shift due to translational motion Δr. The translational motion Δr is related to the translational motion parameters Δr_0 derived from the FatNav registration by $\Delta r = \Delta r_0 + (I - A^{-1}) \times \Delta p$, where I is the unit matrix and Δp is the difference between the TSE and FatNav imaging FOV centers. (5) Because the magnitude images we used possess only real components with zeros phases, the k-space data not acquired due to partial Fourier acceleration at coordinate k was filled by the complex conjugate of data at $-k$. (6) The motion-corrupted images were obtained by applying inverse Fourier transform and then removing the four voxels at each edge of the FOV along PAR direction.

Our motion artifact simulation was performed using motion profiles of all scans in the NoPMC dataset and two baseline images (as shown in Figures S1 and S2) from subjects (named Sub 1 and Sub 2) in the NoPMC dataset with small motion scores (0.87 and 0.80 mm) and no apparent artifacts. The images of subject with the lowest motion score (0.36 mm) were not selected due to the presence of streak artifacts in white matter (denoted by red arrows in Figure S3). For the PMC dataset, our simulation was performed using motion profile and the corresponding image from the same subject as the baseline image. Because there were some residual artifacts on the corrected images, the artifacts on the simulated images may be higher than the images acquired when the PMC is turned off under the same motion condition. Therefore, we also conducted the simulation based on the clean images of Sub 1 and 2. The simulation was implemented in MatLab 2021a (Math-Works, Natick, MA), and each image took approximately 11 min on a computer equipped with 3.3 GHz Intel Xeon W-2275 CPU.

2.3 | **Data analysis**

2.3.1 | Motion parameters

The six rigid-body motion parameters were obtained at each TR either using the 3dvolreg tool in AFNI version 22.3.03[23] (NoPMC dataset) or the MOCO functor (PMC dataset), including rotation and translation around or along left–right (L-R), anterior–posterior (A-P), and superior–inferior (S-I) spatial directions. The registration results of MOCO functor were found to be similar to those obtained using 3dvolreg in AFNI for the same images (difference ≤ 0.037 mm and 0.044 degree in five representative subjects). The motion parameters for the NoPMC dataset were the same as those used in our previous study.[5] The motion profiles were estimated by registering the Fat-Nav images onto the first TR image and subtracted by motion parameters corresponding to time point at which the k-space center was acquired.

To quantify motion severity for each subject, motion score was calculated by summing the root sum square of the translational (M_T, unit: mm) and rotational motion ranges (M_R, unit: degree) along each direction.[5] The value of M_R is roughly equal to the maximum shift (in mm) experienced by a point on the surface of a sphere rotated by M_R degrees with a radius of 57.3 mm, which represents the approximate size of human brain.[24] The motion severity was classified into four groups based on the motion score: no motion (motion score ≤ 0.9 mm), mild (0.9 mm < motion score ≤ 2 mm), moderate (2 mm < motion score ≤ 4 mm), and severe (motion score >4 mm).
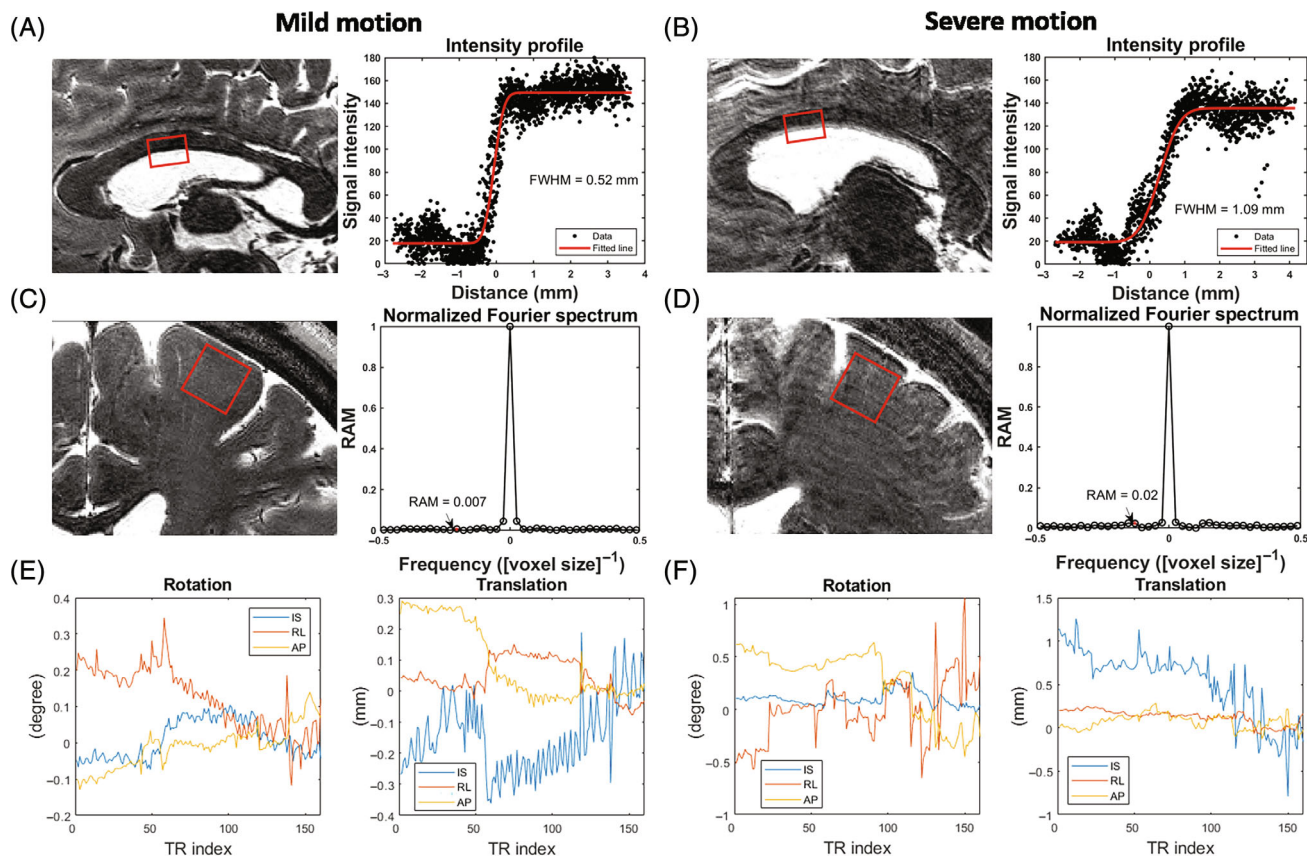
FIGURE 1 Examples of blurring and ringing artifacts on cropped sagittal and coronal slices in real images with mild and severe motion in the NoPMC dataset. (A) and (B) are the lateral ventricle/white matter boundary sharpnesses calculated by the FWHMs of intensity profile estimated from red cuboid ROI. (C) and (D) are RAMs in the normalized Fourier spectrum. (I) and (F) are corresponding motion profiles, with motion scores of 1.25 and 4.19 mm, respectively. NoPMC, without prospective motion correction; RAM, ringing artifact magnitude.

2.3.2 | Blurring artifact measurement: Lateral ventricle/white matter boundary sharpness

Because the goal of the study is to study the effects of motion artifacts on PVS/white matter (WM) visibility, which is dependent on PVS to WM contrast, it is desirable to study how PVS to WM contrast varies with the severity of motion artifacts. However, because the contrast between PVS and WM depends strongly on the partial volume effects, which vary greatly between PVS in different regions and from different subjects,[25] we instead chose to evaluate the effects of motion on image contrast using the sharpness[26] at the lateral ventricle/WM boundary, which should have similar partial volume effects across subjects. Sharpness was quantified using the full width at half maximum (FWHM) of a Gaussian function for which the integral was an s-shaped edge function. The edge function was used to fit the signal variation across tissue boundary. An increase in FWHM was indicative of increased blurriness and decreased image sharpness due to motion.

The region of interest (ROI) for edge function fitting was a cuboid across the lateral ventricular boundary

drawn manually using ITK-SNAP version 3.8[27] on the central sagittal slice with an average size of 7 (S–I) × 3 (L-R) × 6 (A–P) mm^3, as shown by the red rectangles in Figure 1A,B. No interpolation was performed for obtaining the scatter plots in Figure 1. The signal intensities versus the distances of all voxels to the boundary plane were then fitted by the edge function using the lsqcurvefit function in MatLab 2020b (MathWorks) to obtain the FWHM.

2.3.3 | Ringing artifact measurement: Magnitude of high-frequency component in Fourier spectrum

Ringing artifact generates oscillation around tissue boundaries, which manifests as high-frequency components in the frequency domain. Whereas Gibbs ringing artifacts may also appear on high-resolution TSE images as a consequence of finite k-space sampling, such confounding effects produce similar offsets across subjects. Therefore, the magnitude of ringing artifact (RAM) at the oscillation frequency can be used to quantify its level. We used the
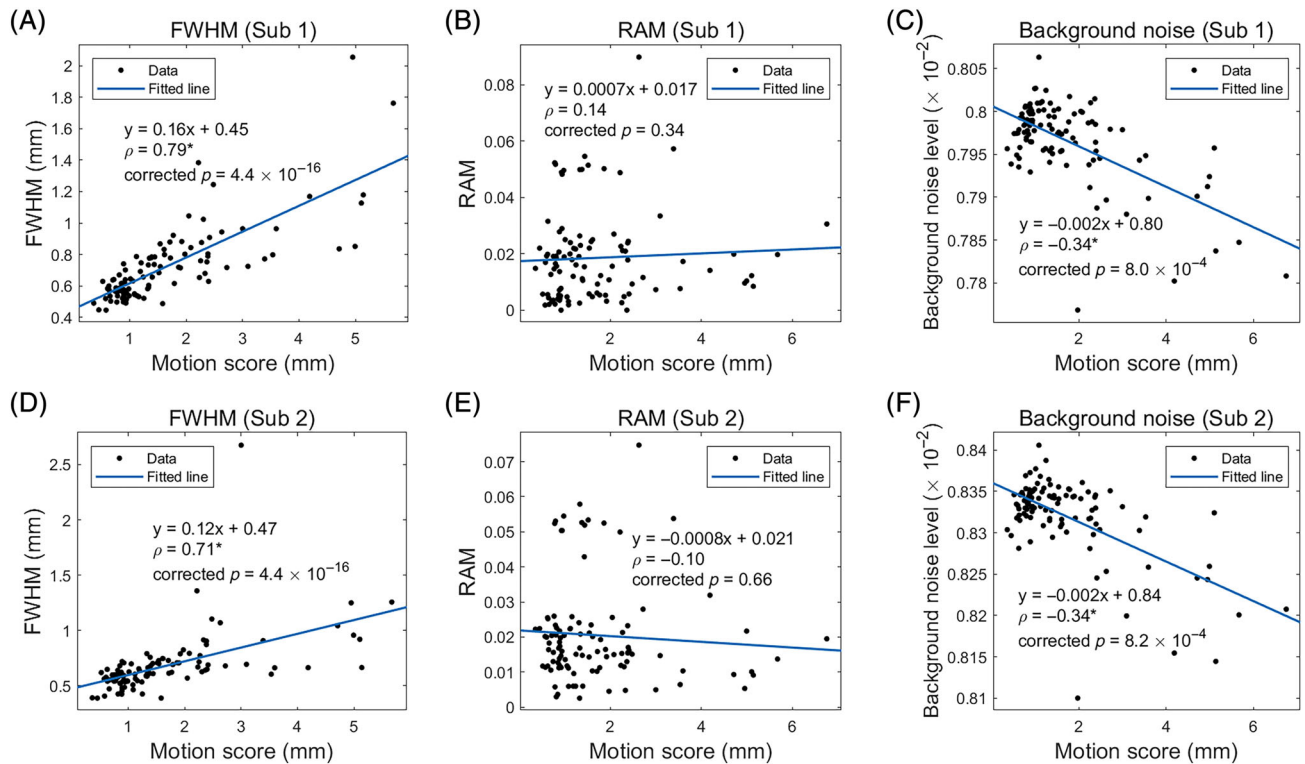
FIGURE 2 Dependencies of motion artifact metrics of simulated images on motion score. Correlations between blurring (A, D), ringing (B, E), and ghosting (C, F) artifact metrics and motion score. The artifact metrics were calculated from the images simulated using motion profiles of the NoPMC and PMC datasets based on the motion-clean images of Sub 1 and 2, respectively. Linear regression coefficients and Spearman correlation coefficients are shown, where asterisks next to the coefficients denote significance ($p < 0.05$). PMC, prospective motion correction.

correlation in RAM between the real and simulated images to assess the validity of ringing artifact simulations.

We first determined the ROI in WM on a coronal slice with an average size of 16 (S–I) $\times$ 16 (L–R) mm^2, where the stripes parallel to the brain surface were prominent, as shown by the red rectangles in Figure 1C,D. The signal intensities along the direction parallel to the stripes were averaged to suppress noise such that the signal oscillation perpendicular to the stripes can be represented by its line intensity profile. The resulting intensity profile was then Fourier transformed to obtain its spectrum in the frequency domain. The magnitudes in spectrum were subsequently normalized to a range of 0–1. To determine the frequency of the ringing artifact, we counted the number of stripes within the ROI and then obtained the magnitude at the corresponding peak position, whose distance to the spectrum center was equal to the number of stripes.

2.3.4 | Ghosting artifact measurement: Background noise level

Ghosting artifact can be considered as a structured noise, which usually appears as a spatial shift of imaged object along the PE direction.[28,29] The presence of ghosting artifact can be examined not only from the overlapping brain structure but also from the background noise level. We determined the background noise level by the standard deviation (SD) of signal intensities across all voxels within 20-mm-wide squares at the four corners of all axial slices. The SDs were normalized by the mean WM signal to account for receiver gain changes across subjects.

2.3.5 | PVS and WM visibility measurement

To quantitatively measure the PVS and WM visibility, a 3D multi-channel multi-scale encoder-decoder network (M^{2}EDN)[30] was applied to delineate tubular PVSs, and a classic encoder–decoder network (U-Net)[31] was applied to segment WM. The WM and PVS volumes were calculated by multiplying the voxel size and the number of segmented voxels. The PVS volume fraction was calculated by the ratio of PVS volume to WM volume.

The maximum intensity projection (MIP) along the viewing A–P and S–I directions of 6 mm-thick sections was calculated to clearly visualize vessel-like thin PVSs.
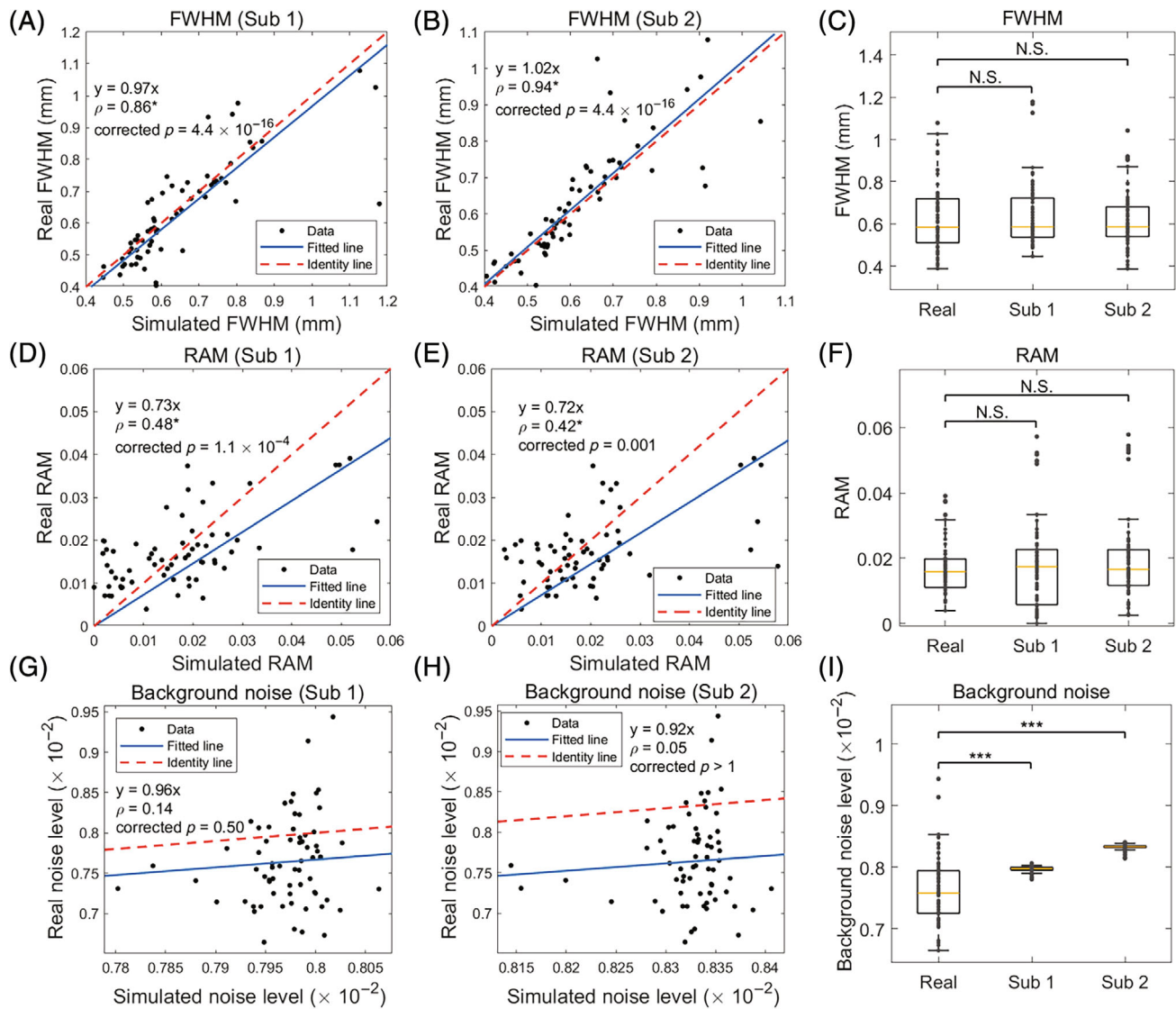
FIGURE 3 Performance of the proposed motion artifact simulation in terms of artifact metrics. Comparison of blurring (A–C), ringing (D–F), and ghosting (G–I) artifact metrics between real and simulated images in the NoPMC dataset. Real images refer to the uncorrected images in the NoPMC dataset from which the motion profiles were obtained. Simulated images were obtained based on these motion profiles and the artifact-free images of Sub 1 and 2, respectively. The red dashed lines denote the identity lines ($y = x$). Linear regression coefficients and Spearman correlation coefficients are shown in the first two columns, where asterisks next to the coefficients denote significance ($p < 0.05$). Wilcoxon signed rank tests were performed in the last column (***$p < 0.001$). N.S., nonsignificance.

2.3.6 | Statistical analysis

Motion scores, FWHMs, RAMs, and background noise level were not normally distributed for the NoPMC dataset in both real and simulated cases ($p \leq 0.007$, Shapiro–Wilk tests). Motion scores, simulated FWHMs, simulated background noise level, and real and simulated RAMs were not normally distributed for the PMC dataset ($p \leq 1.6 \times 10^{-4}$, Shapiro–Wilk tests). WM volume and PVS volume fractions were not normally distributed for the NoPMC and PMC datasets in both real and simulated cases ($p \leq 0.006$, Shapiro–Wilk tests). Due to non-normality, Spearman

correlation test was performed to study the correlation of image metrics between real and simulated images, and between image metrics and motion score. Wilcoxon test was performed to investigate the difference between real and simulated image metrics. However, for studying the correlations between real WM volume and PVS volume fraction and motion score, Spearman partial correlation test was performed instead of Spearman correlation test, taking age (NoPMC) or age and disease (PMC) as confounding factors, both of which have been previously identified as factors that influence PVS visibility.[25,32] Spearman partial correlation tests was not used
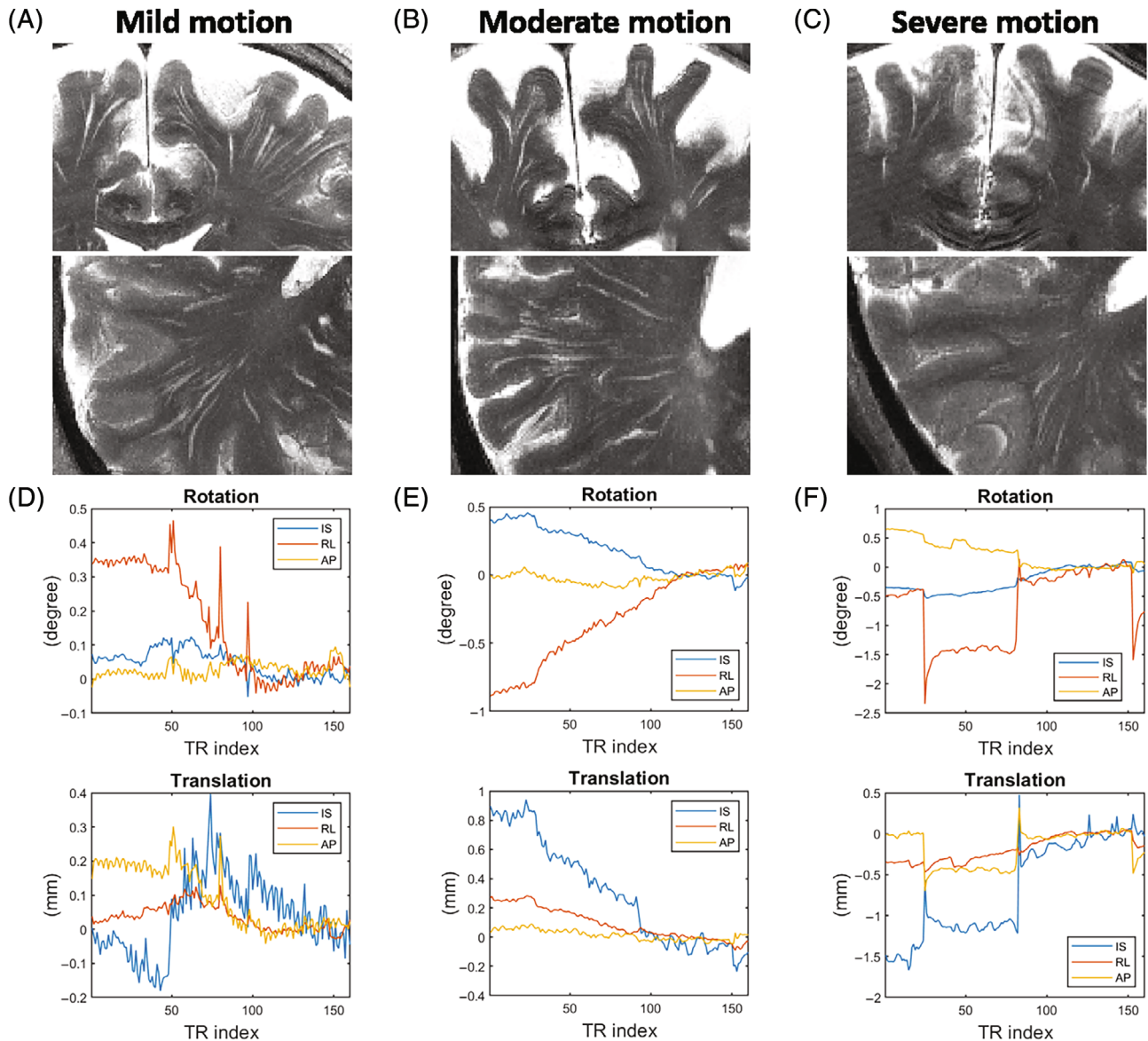
FIGURE 4 Examples of PVS visibility at different motion severities on cropped coronal and axial MIP slices of real NoPMC images. (A–C) are real NoPMC images, with motion scores of 1.24, 2.38, and 5.10 mm and PVS volume fractions of 1.32%, 0.59%, and 0.56%, respectively. (D–F) are corresponding motion profiles. MIP, maximum intensity projection; PVS, perivascular spaces.

for studying the correlations between simulated WM volume/PVS volume fraction and motion score or between real and simulated WM volume/PVS volume fractions because our goal was to test whether motion affects image metrics in the simulated images, which was not affected by age and disease other than through their effects on motion.

The significance threshold was set to 0.05 for p values after corrected by Bonferroni correction to account for multiple comparisons. The statistical analysis was performed using RStudio version 4.2.1 (RStudio, Inc., Boston, MA).

3 | RESULTS

3.1 | Performance of motion artifact simulation

In the NoPMC dataset, the motion score ranged from 0.36 to 5.14 mm, with an average of 1.41 mm ($\pm$1.03 mm). Of the 66 NoPMC images, twenty-nine (43.9%), 22 (33.3%), 11 (16.7%), and 4 (6.1%) belonged to the no, mild, moderate, and severe motion groups, respectively.

Two cases with mild and severe motion in the NoPMC dataset are shown in Figure 1, with motion
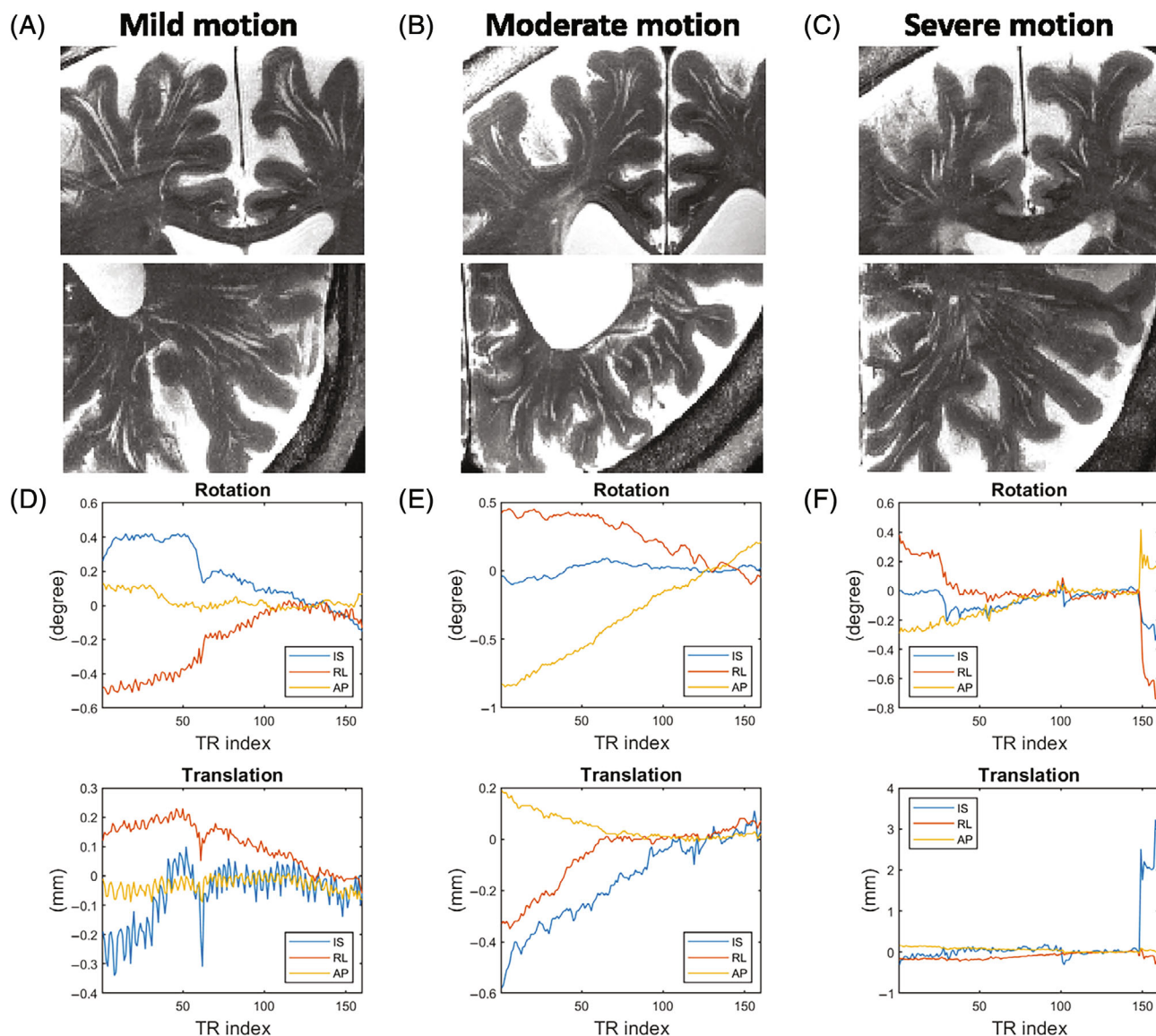
FIGURE 5 Examples of PVS visibility at different motion severities on cropped coronal and axial MIP slices of real PMC images. (A–C) are real PMC images, with motion scores of 1.35, 2.05, and 4.95 mm, and PVS volume fractions of 1.40%, 1.02%, and 1.20%, respectively. (D–F) are corresponding motion profiles.

scores of 1.25 and 4.19 mm, respectively. As the motion severity increased, FWHMs (0.52 and 1.09 mm) also increased as calculated from the image intensity profiles in Figure 1A,B, indicating decreased sharpness at lateral ventricular boundary. Figure 1C,D show the RAMs (0.007 and 0.02) in the normalized Fourier spectrum, suggesting more severe ringing artifacts at large motion. The corresponding motion profiles for the two cases are shown in Figure 1E,F.

Figure 2 shows the correlations between simulated motion artifact metrics and motion score. There were significant positive correlations between FWHMs and motion score ($\rho \geq 0.71$, corrected $p \leq 4.4 \times 10^{-16}$), as shown in Figure 2A,D. However, no significant correlation between simulated RAMs and motion score were found, as shown

in Figure 2B,E (corrected $p \geq 0.34$). There were significant negative correlations between background noise and motion score, as shown in Figure 2C,F ($\rho \leq -0.34$, corrected $p \leq 8.2 \times 10^{-4}$).

The correlations between simulated artifact metrics and motion score only demonstrated the image quality degradation due to motion. To further prove the veracity of simulated artifacts, Figure 3 compares the blurring, ringing, and ghosting artifact metrics between simulated and real NoPMC images. Figure 3A,B reveal that the FWHMs calculated on the real and simulated images were roughly proportional to each other, with the proportionality constants from a linear fit with zero intercept close to identity (0.97 and 1.02, respectively, for
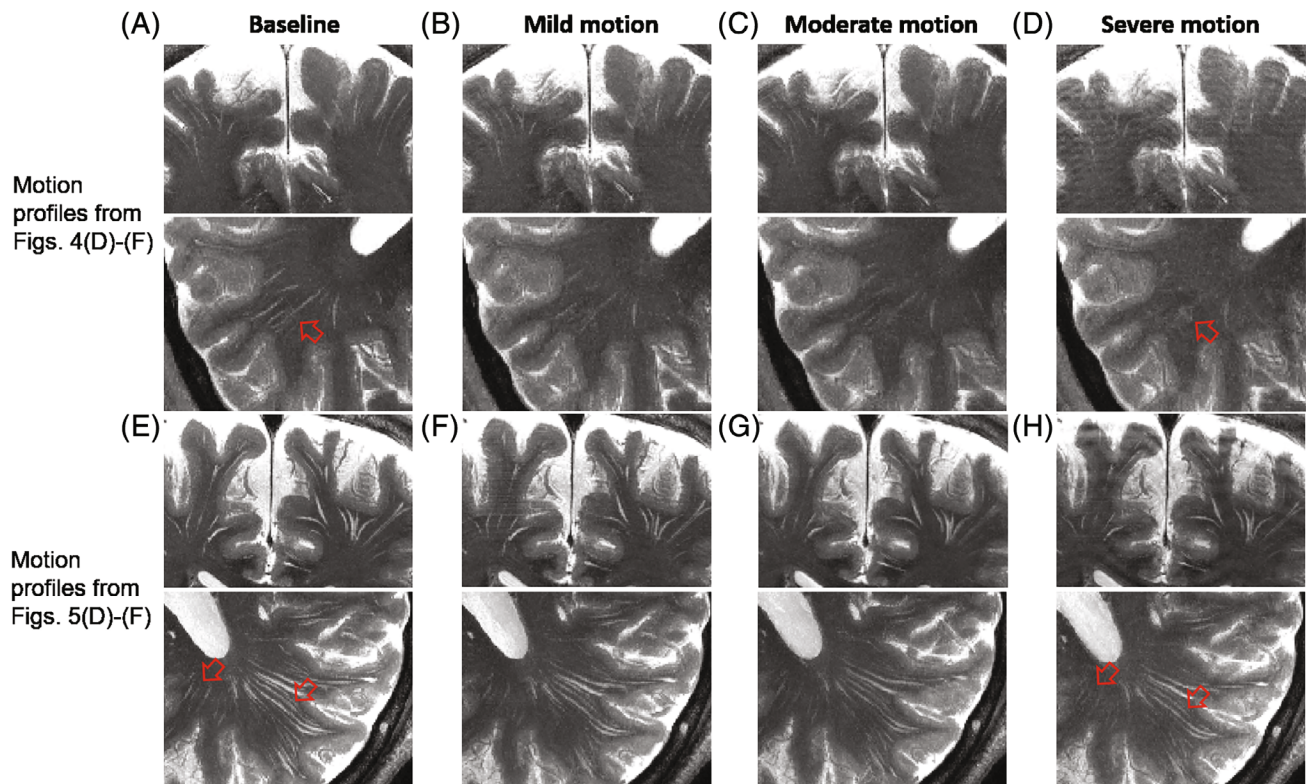
FIGURE 6 Examples of PVS visibility at different motion severities on cropped coronal and axial MIP slices of simulated images. (B–D) were generated by simulation based on the artifact-free image from Sub 1, as shown in (A) and the motion profiles from the NoPMC images in Figure 4D–F, with motion scores of 1.24, 2.38, and 5.10 mm, respectively. (F–H) were generated by simulation based on the artifact-free image from Sub 2, as shown in (E) and the motion profiles from the PMC images in Figure 5D–F, with motion scores of 1.35, 2.05, and 4.95 mm, respectively.

Sub 1 and 2). The Spearman's correlation coefficients were 0.86 and 0.94 (corrected $p \leq 4.4 \times 10^{-16}$), respectively. Figure 3D,E show the weaker but still significant correlations in RAMs between the real and simulated images, with the correlation coefficients of 0.48 and 0.42 (corrected $p \leq 0.001$), respectively. The FWHMs and RAMs were not significantly different between the real and simulated images (Figure 3C,F). However, there was no significant correlation between the simulated and real background noise levels, as shown in Figure 3G,H (corrected $p \geq 0.50$). The background noise was significantly greater in the simulated images than in the real images (Wilcoxon signed rank test; $p \leq 1.4 \times 10^{-5}$), as shown in Figure 3I. The mean values, p values for Wilcoxon signed rank tests, and Spearman correlation coefficients are summarized in rows 1–3 of columns 1–5 in Table S1.

3.2 | Effects of motion artifacts on WM and PVS visibility

To demonstrate the effects of real motion artifacts on PVS visibility at different motion severities with and without

PMC, Figures 4 and 5 show representative real TSE MIP images at different motion severities in the NoPMC and PMC datasets, respectively. For the NoPMC images in Figure 4A–C, the motion scores of the three scans were 1.24, 2.38, and 5.10 mm, respectively, for which the corresponding motion profiles are shown in Figure 4D–F. The PVS/WM boundary became blurrier as the motion score increased. For the PMC images in Figure 5A–C, the motion scores of the three scans were 1.35, 2.05, and 4.95 mm, respectively, for which the corresponding motion profiles are shown in Figure 5D–F. With prospective motion correction, the PVS/WM boundary still remained clearly defined despite the presence of some ringing artifacts.

To demonstrate the effects of simulated motion artifacts on PVS visibility at different motion severities, Figure 6B–D,F–H display the MIP of the simulated images generated using the motion profiles in Figures 4 and 5, and the baseline images of Sub 1 and 2 (shown in Figure 6A,E, respectively). There was a clear decrease of PVS visibility as the motion score increased in both datasets, as denoted by red arrows, because the PMC effects were not considered in the simulation. The original PVS volume fraction of Sub
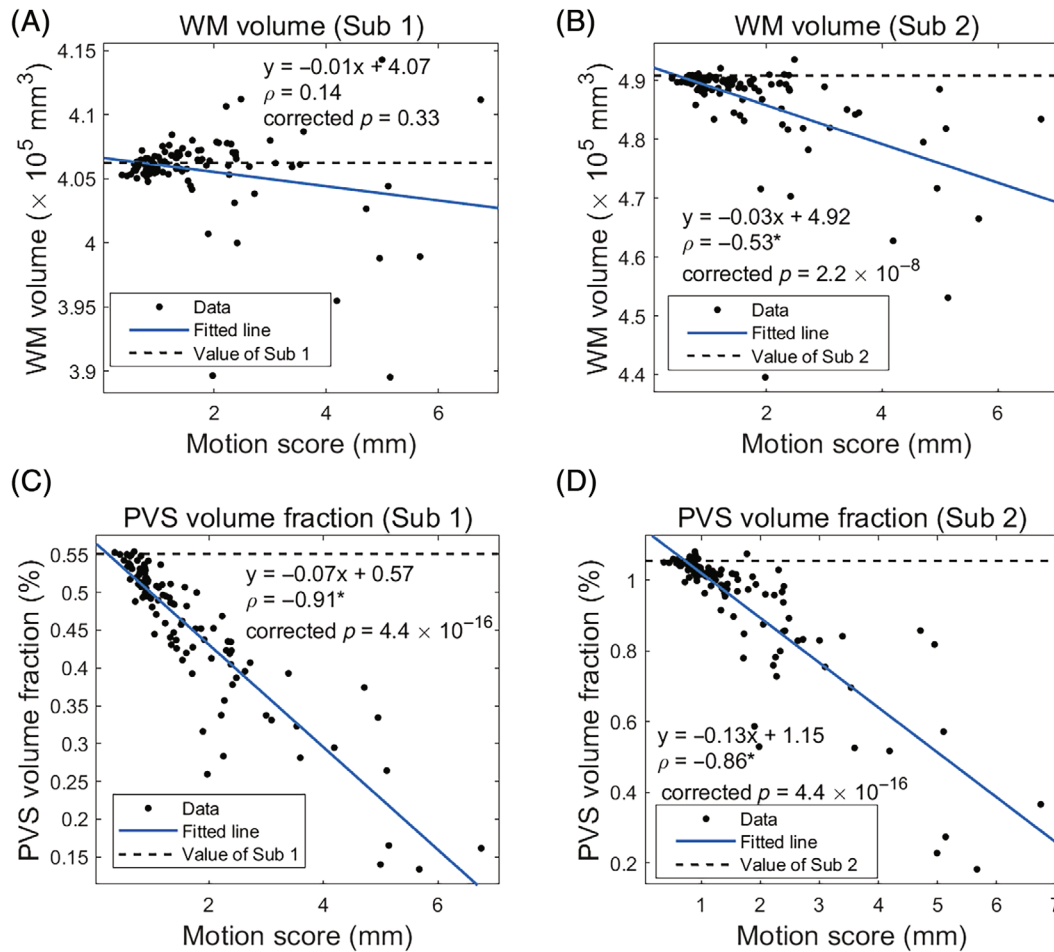
FIGURE 7 Effects of simulated motion artifacts on WM volume (A, B) and PVS volume fraction (C, D). The WM and PVS metrics were obtained from the images simulated using motion profiles of the NoPMC and PMC datasets based on the artifact-free images of Sub 1 and 2, respectively. The black dashed lines denote the values calculated from the baseline images. Linear regression coefficients and Spearman correlation coefficients are shown, where asterisks next to the coefficients denote significance ($p < 0.05$). WM, white matter.

1 (Sub 2) was 0.55% (1.05%). After simulation, the volume fractions became 0.46% (0.97%), 0.40% (0.88%), and 0.26% (0.82%), respectively, as the motion severity increased.

Figure 7 shows the dependencies of WM volume and PVS volume fraction on the motion score calculated from the simulated images for Sub 1 and 2. For the WM volume, significant negative correlation was found for Sub 2 ($\rho = -0.53$, corrected $p = 2.2 \times 10^{-8}$) but not for Sub 1. For the PVS volume fraction, strong negative correlations were observed for both subjects ($\rho \leq -0.86$, corrected $p \leq 4.4 \times 10^{-16}$). Additionally, there was no significant correlation between real WM volume and motion score (data not shown; $\rho = -0.03$, corrected $p > 1$) or between real PVS volume fraction and motion score (data not shown; $\rho = -0.27$, corrected $p = 0.08$) in the NoPMC dataset.

No significant correlation between real and simulated WM volumes was observed in the NoPMC dataset, as shown in Figure 8A,B. However, in contrast to a lack of correlation between real PVS volume fraction and motion

score, there were significant correlations between real and simulated PVS volume fraction ($\rho \geq 0.36$, corrected $p \leq 0.006$) in the NoPMC dataset, as shown in Figure 8D,E. The Wilcoxon test was not performed in Figure 8C,F because the real images were from different subjects, whereas the simulated images were from two representative subjects. The mean values of the WM volume and PVS volume fraction and Spearman correlation coefficients between real and simulated images are summarized in rows 4–5 of columns 1–5 in Table S1.

3.3 | Performance of prospective motion correction

In the PMC dataset, the motion score ranged from 0.70 to 6.75 mm, with an average of 2.12 mm (± 1.37 mm). Of the 38 PMC images, three (7.9%), 21 (55.3%), 10 (26.3%), and four (10.5%) belonged to the no, mild, moderate, and severe motion groups, respectively. The motion
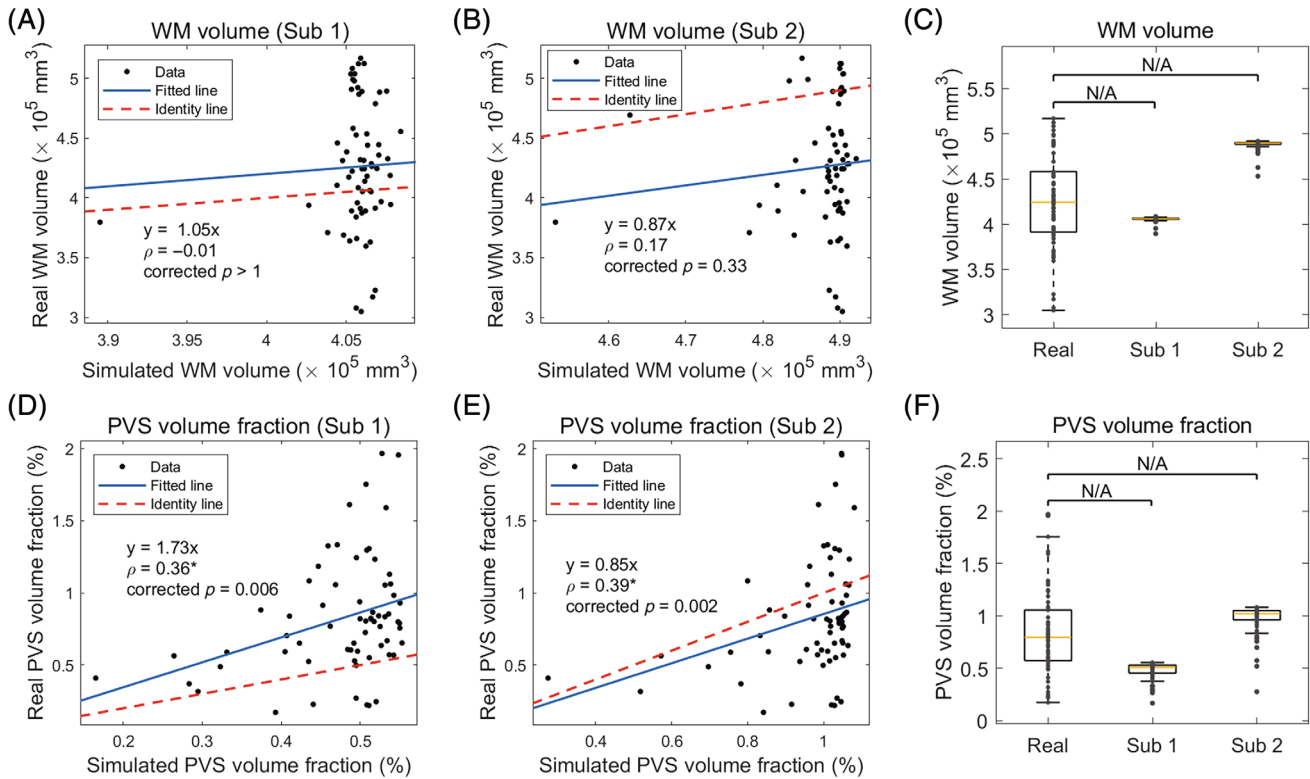
FIGURE 8 Comparison of WM volume (A–C) and PVS volume fraction (D–F) between real and simulated images in the NoPMC dataset. Real images refer to the uncorrected images in the NoPMC dataset from which the motion profiles were obtained. Simulated images were obtained based on these motion profiles and the artifact-free images of Sub 1 and 2, respectively. The red dashed lines denote the identity lines ($y = x$). Linear regression coefficients and Spearman correlation coefficients are shown in the first two columns, where asterisks next to the coefficients denote significance ($p < 0.05$). Wilcoxon signed rank tests were not performed in the last column. N/A, not available.

scores of PMC dataset were significantly higher than those of NoPMC dataset, as shown in Figure S4A (Wilcoxon rank sum test; $p \leq 0.02$). However, the motion scores were not significantly different between the patients and healthy controls in the PMC dataset (Wilcoxon rank sum test; $p = 0.22$). Besides, the PVS volume fractions of patients in the PMC dataset were significantly higher than those of healthy volunteers in both NoPMC and PMC datasets, as shown in Figure S4B (Wilcoxon rank sum test; $p \leq 0.01$).

Figure 9 compares the FWHM, RAM, background noise, WM volume, and PVS volume fraction between real and simulated images in the PMC dataset, when the simulation was conducted based on the corrected images. There were significant correlations in all the metrics between real and simulated images ($p \leq 0.03$). The real FWHMs and RAMs were lower (slope ≤ 0.90), whereas the real PVS volume fractions were higher than the simulated ones (slope $= 1.16$). Furthermore, the boxplots on Figure 9B,J also show the significantly reduced FWHMs and the significantly increased PVS volume fractions on the corrected images as compared to the simulated images (Wilcoxon signed rank test; $p \leq 1.5 \times 10^{-7}$). However, Figure 9F

shows the significantly increased background noise on the corrected images as compared to the simulated images. No significant difference between the simulated and real images was observed for RAM and WM volume, as shown in Figure 9D,H. The mean values of the metrics, p values for Wilcoxon signed rank tests, and Spearman correlation coefficients are summarized in Table S2.

Figure 10 compares the FWHM, RAM, and PVS volume fraction between real and simulated images in the PMC dataset, when the simulation was conducted based on the images of Sub 1 and 2. In contrast to the NoPMC dataset, there was no significant correlation for any of the three metrics (corrected $p \geq 0.48$) or background noise (data not shown; corrected $p \geq 0.10$) between real and simulated images, suggesting the reduction of motion effects with prospective motion correction. Furthermore, significantly lower FWHMs (Figure 10C) were found on the real images than on the simulated images (Wilcoxon signed rank test; $p \leq 1.7 \times 10^{-7}$), suggesting the improving sharpness after prospective motion correction. The mean values of the metrics, p values for Wilcoxon signed rank tests, and Spearman correlation coefficients are summarized in columns 6–10 of Table S1.
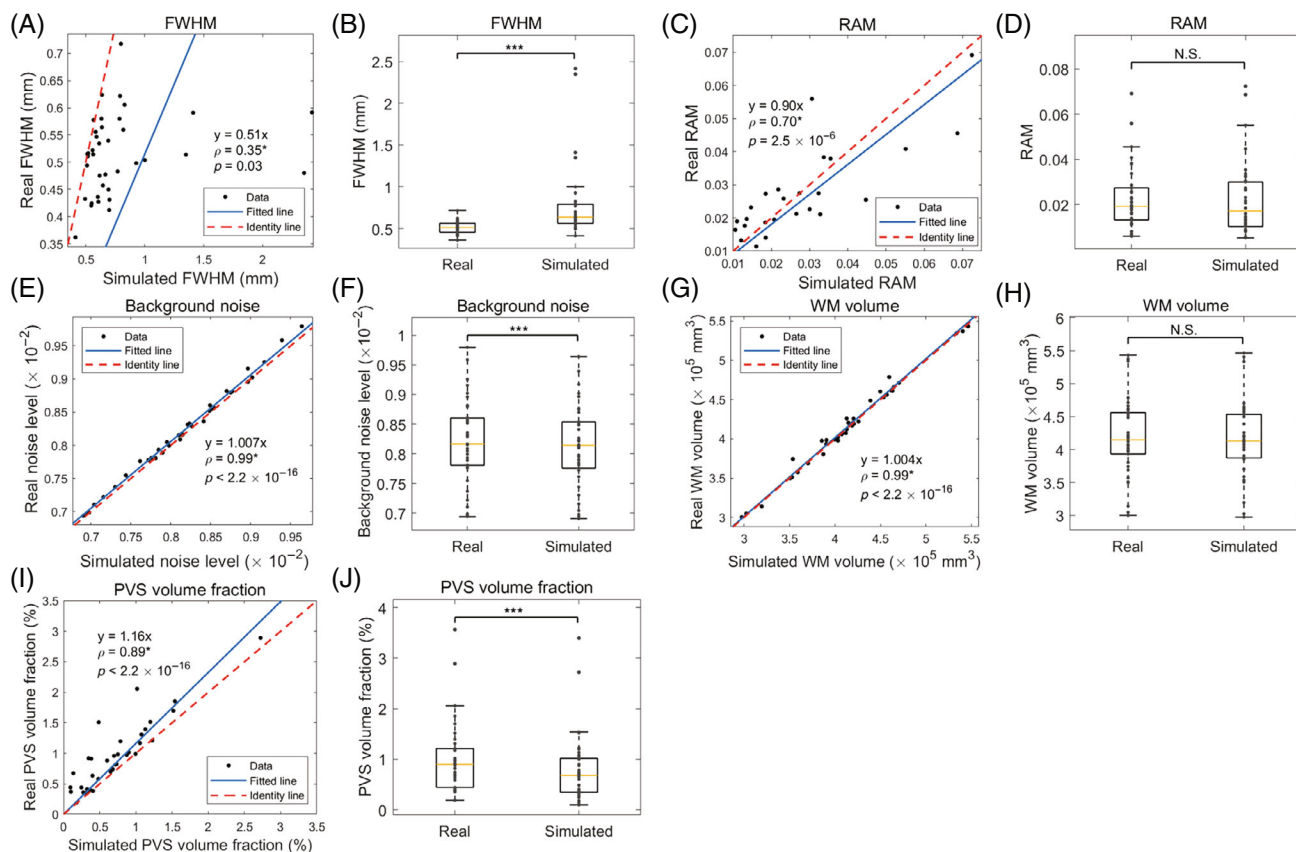
FIGURE 9 Comparison of blurring artifact (A, B), ringing artifact (C, D), ghosting artifact (E, F), WM volume (G, H), and PVS volume fraction (I, J) between real and simulated images in the PMC dataset. Real images refer to the prospectively motion corrected images in the PMC dataset from which the motion profiles were obtained. Simulated images were obtained based on these motion profile and the corresponding PMC image from the same subject. The red dashed lines denote the identity lines ($y = x$). Linear regression coefficients and Spearman correlation coefficients are shown in the first and third columns, where asterisks next to the coefficients denote significance ($p < 0.05$). Wilcoxon signed rank tests were performed in the second and last columns (***$p < 0.001$). N.S., nonsignificance.

4 | DISCUSSION

In this study, we proposed motion artifact simulation to measure the effects of PMC on PVSs. This method allows for generation of uncorrected images to evaluate the PMC performance without the need of MR scan repetition. We found that FWHM, RAM, and PVS volume fraction were significantly correlated between simulated and real images in the NoPMC dataset, suggesting the effectiveness of the simulation approach in reproducing blurring and ringing artifacts and PVS visibility reduction. Such correlations were absent in the PMC dataset, suggesting the ability of PMC to alleviate motion artifacts on real images. Furthermore, we found that PMC can improve image sharpness in the presence of motion.

Several methods have been proposed to obtain the uncorrected images in order to assess the performance of PMC, including acquired multiple scans with PMC enabled and disabled,[10–17] and motion artifact simulation.[18] However, to evaluate the effectiveness of PMC in routine clinical studies, motion artifact simulation is more feasible. Multiple scans and interleaved acquisition will prolong the scan time that affects the comfort level of subjects and increases the likelihood of head movements. Furthermore, in methods using multiple scans, the motion observed in each scan cannot be identical, although usually the subjects are instructed to perform deliberate movements.[13–16] In addition, the effectiveness of PMC on correcting intentional motion-induced artifacts may not be generalizable to routine studies in which more complex unintentional motion can occur.

Multiple methods have been proposed for performing motion artifact simulation,[33] including those based on magnitude images[6–9] and those based on multi-channel complex k-space data.[18,34] Magnitude image-based methods require less computational time and are applicable to more studies because the raw k-space data are not always available. Motion effects were accounted for by either modifying k-space coordinates while keeping the data intact[8,18,34] or by modifying the k-space data at the
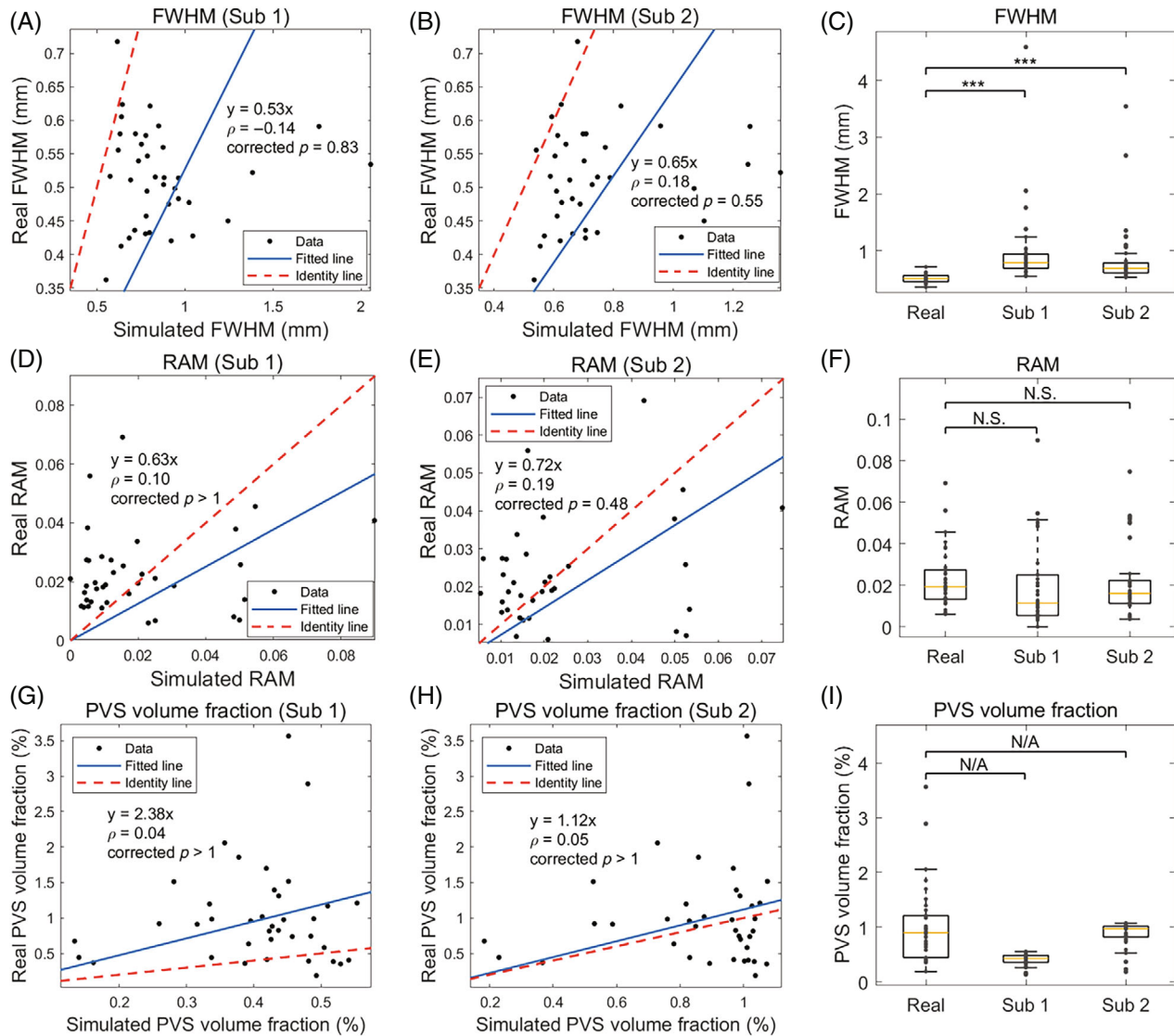
FIGURE 10 Comparison of blurring artifact metrics (A–C), ringing artifact metrics (D–F), and PVS volume fraction (G–I) between real and simulated images in the PMC dataset. Real images refer to the prospectively motion corrected images in the PMC dataset from which the motion profiles were obtained. Simulated images were obtained based on these motion profiles and the artifac-free images of Sub 1 and 2, respectively. The red dashed lines denote the identity lines ($y = x$). Linear regression coefficients and Spearman correlation coefficients are shown, where asterisks next to the coefficients denote significance ($p < 0.05$). Wilcoxon signed rank tests were performed in (C) and (F) (***$p < 0.001$).

same coordinates.[6–9] We adopted the latter approach since it matches more closer to the actual data sampling and image reconstruction process in the presence of motion. To the best of our knowledge, our method of calculating motion-corrupted data directly using nonuniform fast Fourier transform has not been proposed in the earlier studies.[6–9] Furthermore, the method of using realistic motion profiles to simulate artifacts and comparing them to the artifacts in the corresponding real images has not been carried out, except for a study by Zahneisen et al.[18]

The RAM in simulated images shows a nonsignificant correlation with motion score (Figure 2B,E)

but significantly correlated with RAM in real images (Figure 3D,E). Furthermore, the PVS volume fraction in real NoPMC images shows a nonsignificant negative correlation with motion score but a significant positive correlation with the simulated PVS volume fraction (Figure 8D,E). These suggest that our motion simulation can more accurately reflect the effects of motion on the PVS visibility than the motion score, as the artifact level depends not only on motion range but also motion pattern.

The significant correlations in FWHM, RAM, and PVS volume fraction between simulated and real images across subjects in NoPMC dataset (Table S1) further demonstrate

the veracity of the simulated motion-induced artifacts. Such correlations were reduced and became nonsignificant if the real NoPMC images were replaced by the PMC images. Furthermore, we found a significant reduction in FWHMs on real PMC images compared to simulated images. These suggest the effectiveness of PMC in mitigating the negative effects of motion on image sharpness and PVS visibility. However, the differences between real and simulated RAMs were nonsignificant in the PMC dataset, which implied that PMC was less effective in reducing ringing artifacts compared to blurring artifacts.

In contrast to the PVS volume fraction, the correlations of WM volume between real and simulated images were weaker (Figure 8A,B), which suggest the lower sensitivity of WM visibility to motion than the smaller thin-tubular structures such as PVS. In addition, we found the nonsignificant correlations between simulated and real background noise level (Figure 3G,H), suggesting the dominance of other noise sources such as thermal and physiological noises that our simulation was not capable of reproducing.

Several studies have identified PVS as a potential biomarker of neurovascular and neurodegenerative diseases.[2,35–38] PVS play a crucial role in the removal of metabolic substances and waste products from brain. Its abnormalities can lead to the accumulation of toxins and wastes, which may contribute to the pathogenesis of these diseases. The improvements in PVS visibility and robustness against motion on MRI by PMC can facilitate the investigation of PVS abnormalities, especially in longitudinal studies, which may provide novel insights into the underlying neuropathogenesis and promote the development of therapeutic targets.

There are several limitations of our study. First, no real images with and without motion from the same subjects were used for validating the simulation method. Second, although the computation demand can be considerably reduced, the difference in simulation performance conducted on the k-space of magnitude image or the raw k-space data remain to be studied. Furthermore, the simulation neglected the potential impacts of magnetic field inhomogeneity and RF transmitting and receiving coil sensitivities, which might change due to head position and orientation during the scan. The resulting MR signal variations could lead to deviations of simulated artifacts.

5 | CONCLUSIONS

Our proposed motion artifact simulation provides an effective tool for investigating the effects of motion and PMC on PVS visibility. In the presence of motion, the FatNav-based PMC was shown to mitigate the negative impacts of motion and increase the volume of MRI-visible PVSs in WM. Our study demonstrated the value of PMC for improving the quality of PVS images in investigations aimed at further illuminating the potential role of PVS abnormalities in the pathogenesis of neurodegenerative disorder.

DATA AVAILABILITY STATEMENT

The Matlab codes for artifact simulation are available in Mendeley Data (https://data.mendeley.com/datasets/xn7zmt2rxy/3).

ORCID

Bingbing Zhao https://orcid.org/0009-0001-1638-0736
Xiaopeng Zong https://orcid.org/0000-0003-4235-6948

REFERENCES

1. Bohr T, Hjorth PG, Holst SC, et al. The glymphatic system: current understanding and modeling. *iScience*. 2022;25:104987.
2. Ramirez J, Berezuk C, McNeely AA, Gao F, McLaurin J, Black SE. Imaging the perivascular space as a potential biomarker of neurovascular and neurodegenerative diseases. *Cell Mol Neurobiol*. 2016;36:289-299.
3. Bellon EM, Haacke EM, Coleman PE, Sacco DC, Steiger DA, Gangarosa RE. MR artifacts: a review. *AJR Am J Roentgenol*. 1986;147:1271-1281.
4. Zaitsev M, Maclaren J, Herbst M. Motion artifacts in MRI: a complex problem with many partial solutions. *J Magn Reson Imaging*. 2015;42:887-901.
5. Zong X, Nanavati S, Hung SC, Li T, Lin W. Effects of motion and retrospective motion correction on the visualization and quantification of perivascular spaces in ultrahigh resolution T2-weighted images at 7T. *Magn Reson Med*. 2021;86:1944-1955.
6. Johnson PM, Drangova M. Conditional generative adversarial network for 3D rigid-body motion correction in MRI. *Magn Reson Med*. 2019;82:901-910.
7. Preetha CJ, Mattern H, Juneja M, Vogt J, Speck O, Hartkens T. Entropy-based SVM classifierclassifier for automatic detection of motion artifacts in clinical MRI. *Bildverarbeitung für Die Medizin*. 2020;2020:107-112.
8. Duffy BA, Zhao L, Sepehrband F, et al. Retrospective motion artifact correction of structural MRI images using deep learning improves the quality of cortical surface reconstructions. *Neuroimage*. 2021;230:117756.
9. Pawar K, Chen Z, Shah NJ, Egan GF. Suppressing motion artefacts in MRI using an inception-ResNet network with motion simulation augmentation. *NMR Biomed*. 2022;35:e4225.

10. Herbst M, Maclaren J, Lovell-Smith C, et al. Reproduction of motion artifacts for performance analysis of prospective motion correction in MRI. *Magn Reson Med*. 2014;71:182-190.

11. Nael K, Pawha PS, Fleysher L, et al. Prospective motion correction for brain MRI using an external tracking system. *J Neuroimaging*. 2021;31:57-61.

12. Sciarra A, Mattern H, Yakupov R, et al. Quantitative evaluation of prospective motion correction in healthy subjects at 7T MRI. *Magn Reson Med*. 2022;87:646-657.

13. Forman C, Aksoy M, Hornegger J, Bammer R. Self-encoded marker for optical prospective head motion correction in MRI. *Med Image Anal*. 2011;15:708-719.

14. White N, Roddey C, Shankaranarayanan A, et al. PROMO: real-time prospective motion correction in MRI using image-based tracking. *Magn Reson Med*. 2010;63:91-105.

15. Bayih SG, Jankiewicz M, Alhamud A, van der Kouwe AJW, Meintjes EM. Self-navigated prospective motion correction for 3D-EPI acquisition. *Magn Reson Med*. 2022;88:211-223.

16. Gao X, Hucker P, Hennig J, Zaitsev M. Strategies to improve intratrain prospective motion correction for turbo spin-echo sequences with constant flip angles. *Magn Reson Med*. 2021;86:852-865.

17. Schulz J, Siegert T, Reimer E, et al. An embedded optical tracking system for motion-corrected magnetic resonance imaging at 7T. *MAGMA*. 2012;25:443-453.

18. Zahneisen B, Keating B, Singh A, Herbst M, Ernst T. Reverse retrospective motion correction. *Magn Reson Med*. 2016;75:2341-2349.

19. Zong X, Jimenez J, Li T, Powers WJ. In vivo detection of penetrating arteriole alterations in cerebral white matter in patients with diabetes with 7 T MRI. *Magn Reson Imaging*. 2023;100:84-92.

20. Gallichan D, Marques JP, Gruetter R. Retrospective correction of involuntary microscopic head movement using highly accelerated fat image navigators (3D FatNavs) at 7T. *Magn Reson Med*. 2016;75:1030-1039.

21. Griswold MA, Jakob PM, Heidemann RM, et al. Generalized autocalibrating partially parallel acquisitions (GRAPPA). *Magn Reson Med*. 2002;47:1202-1210.

22. Fessler JA, Sutton BP. Nonuniform fast Fourier transforms using min-max interpolation. *IEEE Trans Signal Process*. 2003;51:560-574.

23. Cox RW. AFNI: software for analysis and visualization of functional magnetic resonance neuroimages. *Comput Biomed Res*. 1996;29:162-173.

24. Moore J, Jimenez J, Lin W, Powers W, Zong X. Prospective motion correction and automatic segmentation of penetrating arteries in phase contrast MRI at 7 T. *Magn Reson Med*. 2022;88:2088-2100.

25. Zong X, Lian C, Jimenez J, Yamashita K, Shen D, Lin W. Morphology of perivascular spaces and enclosed blood vessels in young to middle-aged healthy adults at 7T: dependences on age, brain region, and breathing gas. *Neuroimage*. 2020;218:116978.

26. Bazin PL, Nijsse HE, van der Zwaag W, et al. Sharpness in motion corrected quantitative imaging at 7T. *Neuroimage*. 2020;222:117227.

27. Yushkevich PA, Piven J, Hazlett HC, et al. User-guided 3D active contour segmentation of anatomical structures: significantly improved efficiency and reliability. *Neuroimage*. 2006;31:1116-1128.

28. Wood ML, Henkelman RM. MR image artifacts from periodic motion. *Med Phys*. 1985;12:143-151.

29. Liu H, Koonen J, Fuderer M, Heynderickx I. The relative impact of ghosting and noise on the perceived quality of MR images. *IEEE Trans Image Process*. 2016;25:3087-3098.

30. Lian C, Zhang J, Liu M, et al. Multi-channel multi-scale fully convolutional network for 3D perivascular spaces segmentation in 7T MR images. *Med Image Anal*. 2018;46:106-117.

31. Ronneberger O, Fischer P, Brox T. U-Net: convolutional networks for biomedical image segmentation. In: Navab N, Hornegger J, Wells W, Frangi A, eds. *Medical Image Computing and Computer-Assisted Intervention – MICCAI 2015. Lecture Notes in Computer Science vol 9351*. Springer; 2015.

32. Wang S, Huang P, Zhang R, et al. Quantity and morphology of perivascular spaces: associations with vascular risk factors and cerebral small vessel disease. *J Magn Reson Imaging*. 2021;54:1326-1336.

33. Spieker V, Eichhorn H, Hammernik K, et al. Deep learning for retrospective motion correction in MRI: a comprehensive review. *IEEE Trans Med Imaging*. 2024;43:846-859.

34. Preboske GM, Gunter JL, Ward CP, Jack CR. Common MRI acquisition non-idealities significantly impact the output of the boundary shift integral method of measuring brain atrophy on serial MRI. *Neuroimage*. 2006;30:1196-1202.

35. Charidimou A, Jaunmuktane Z, Baron JC, et al. White matter perivascular spaces: an MRI marker in pathology-proven cerebral amyloid angiopathy? *Neurology*. 2013;82:57-62.

36. Brown R, Benveniste H, Black SE, et al. Understanding the role of the perivascular space in cerebral small vessel disease. *Cardiovasc Res*. 2018;114:1462-1473.

37. Ramirez J, Berberian SA, Breen DP, et al. Small and large magnetic resonance imaging-visible perivascular spaces in the basal ganglia of Parkinson's disease patients. *Mov Disord*. 2022;37:1304-1309.

38. Plog BA, Nedergaard M. The glymphatic system in central nervous system health and disease: past, present, and future. *Annu Rev Pathol*. 2018;13:379-394.

SUPPORTING INFORMATION

Additional supporting information may be found in the online version of the article at the publisher's website.

FIGURE S1. Magnitude images of Sub 1 from NoPMC dataset and corresponding motion profile with the motion score of 0.87 mm.

FIGURE S2. Magnitude images of Sub 2 from NoPMC dataset and corresponding motion profile with the motion score of 0.80 mm.

FIGURE S3. Magnitude images of a subject from NoPMC dataset and corresponding motion profile that had the lowest motion score of 0.36 mm. This subject image was not selected as the baseline for simulation due to the observed streak artifacts denoted by red arrows.

FIGURE S4. Comparison of motion scores (A) and PVS volume fractions (B) between healthy volunteers and diabetes. NoPMC dataset contain 66 images of 33 healthy volunteers. PMC dataset contain 19 images of healthy

volunteers and 19 images of diabetes. The *p* values for Wilcoxon's rank sum tests are shown.

TABLE S1. Mean values of the image metrics of real and simulated images in the NoPMC and PMC datasets, *p* values of Wilcoxon's signed rank tests and Spearman's correlation tests between them. Simulation was conducted based on the motion-clean images of Sub 1 and 2. The p values were all corrected using Bonferroni correction.

TABLE S2. Mean values of the image metrics of real and simulated images in the PMC dataset, *p* values of Wilcoxon's signed rank tests and Spearman's correlation

tests between them. Simulation was conducted based on the motion profile and corresponding image from the same subject.